



This is a repository copy of *Physics-informed deep learning for modelling particle aggregation and breakage processes*.

White Rose Research Online URL for this paper:
<https://eprints.whiterose.ac.uk/180855/>

Version: Accepted Version

Article:

Chen, X. orcid.org/0000-0001-8073-5741, Wang, L.G., Meng, F. et al. (1 more author) (2021) Physics-informed deep learning for modelling particle aggregation and breakage processes. *Chemical Engineering Journal*, 426. 131220. ISSN 1385-8947

<https://doi.org/10.1016/j.cej.2021.131220>

Article available under the terms of the CC-BY-NC-ND licence
(<https://creativecommons.org/licenses/by-nc-nd/4.0/>).

Reuse

This article is distributed under the terms of the Creative Commons Attribution-NonCommercial-NoDerivs (CC BY-NC-ND) licence. This licence only allows you to download this work and share it with others as long as you credit the authors, but you can't change the article in any way or use it commercially. More information and the full terms of the licence here: <https://creativecommons.org/licenses/>

Takedown

If you consider content in White Rose Research Online to be in breach of UK law, please notify us by emailing eprints@whiterose.ac.uk including the URL of the record and the reason for the withdrawal request.



eprints@whiterose.ac.uk
<https://eprints.whiterose.ac.uk/>

1 **Keywords:** Physics-Informed Neural Network; Population balance equation; Aggregation;
2 Breakage; Inverse problem; Parameter estimation

3 **1. Introduction**

4 Population balance model (PBM) is widely used for modelling particulate systems in a variety
5 of applications such as crystallizations, millings, polymerization and granulations [1-6]. PBM
6 can quantify how a distribution of particle descriptors changes over the studied time based on
7 kernel functions representing the relevant mechanisms that affect the particle evolutions. It can
8 also be coupled to computational fluid dynamics where the spatial evolution of particle
9 descriptors can be tracked [7-10]. However, the model consists of highly nonlinear integral-
10 partial different equations, which usually needs to be solved numerically. Until now, various
11 numerical techniques are therefore developed to solve it, including the method of class [11],
12 moment methods [12, 13], Monte Carlo methods [14] and meshless radial basis method [15].
13 Hounslow et al. (1988) and Litster et al. (1995) developed a discretization procedure for the
14 aggregation problems using the method of class. This method was extended to solve breakage
15 problem by Vanni (2000). Kumar and Ramkrishna (1996) developed a method of
16 discretization with a pivot technique that involves a selective refinement of a relatively coarse
17 grid. The number of sections is kept to a minimum and they have shown that the method can
18 be successfully applied to agglomeration/breakage problems. A recent review of the solutions
19 of population balance equations for simulating disperse multiphase flows is given by Shiea,
20 Buffo, Vanni and Marchisio [16]. However, the existing numerical schemes are designed to
21 solve the forward problems of population balance equation but are difficult to deal with the
22 inverse problems. Many real-world applications of PBM need to be formulated as inverse
23 modelling problems, which are to identify a set of parameters or functions to make the outputs
24 of forward analysis match the desired results or measurements. The calibration or search of the

1 optimal kernel parameters of the population balance model using the existing schemes still
2 needs massive additional efforts.

3 Over the past few years, there has been a revolution in the successful application of deep
4 learning in various fields such as computer vision, natural language processing, image
5 classification and recognition. Despite its great success in these fields, applying deep learning
6 in the field of physics-based particulate systems is relatively scarce. Physical processes can
7 usually be described by conservation laws with dynamic and kinematic constraints represented
8 through a set of ordinary or partial differential equations. Machine learning has the capabilities
9 in learning complex representations of data and approximating physical processes, which
10 provides the potential to solve the challenging open problems of physical systems. For example,
11 in the wet granulation process, the underlying physics are not completely available (e.g. the
12 breakage and agglomeration mechanisms). However, some extra information from the
13 experimental data could be available for machine learning methods to explore. By integrating
14 the information from both physics and data exploitation through machine learning methods, it
15 will be well positioned to recover and identify the particle kinetic in a complex process such
16 as granulation, milling and crystallisation. In recent years, the scientific machine learning
17 method [17] is being actively explored to solve these problems. The method can be trained
18 with both experimental and numerical data, which shows a great potential to optimize the
19 complicated industrial processes. Particularly, the physics informed neural network (PINN)
20 method has attracted much attention [18-20]. PINN endows a neural network model with
21 known equations that govern the physics of a system [19, 21]. In addition to training data, the
22 governing equations, as well as initial and boundary conditions of a mechanistic model can be
23 embedded in the cost function of PINN. The method has been proven to be very successful in
24 solving systems of ordinary differential equations and partial differential equations, such as
25 Schrodinger, Allen-Cahn and Navier-Stokes equations [22]. Moreover, the method is also

1 shown to be applicable in solving both forward and inverse problems of differential equations
2 systems, which can overcome the limitations of existing numerical methods and is promising to
3 be applied in a wide range of physical systems [19].

4 In this study, we develop a physics-informed deep learning framework to solve both forward
5 and inverse problems of the population balance model that describes and predicts the particle
6 distribution undergoing aggregation and breakage. The governing equations of the population
7 balance model is directly integrated into the loss function of a neural network to penalise the
8 unphysical predictions so that the framework can be trained efficiently and fulfils physical
9 constraints. The key advantage of such model structure is its interpretability and generalization
10 for various particulate processes. To demonstrate the feasibility of physics-informed deep
11 learning framework, cases with simple kernels are studied in the forward problems since
12 analytical solutions are available for training. A laboratory ball mill with sparse experimental
13 data will be used to test the performance of the framework for solving inverse problems. The
14 paper is structured as follows. The mathematical theory is described in section 2. Exemplar
15 forward solutions and model parameter discovery of population balance equations with
16 simulation results are given in section 3. Finally, conclusions and future work are given in
17 section 4.

18

19 **2. Mathematical model**

20 **2.1 Population balance equations**

21 Considering a well-mixed system of particles that undergo aggregation and breakage, the
22 population balance equation can be written as below

$$\begin{aligned} \frac{dN(v,t)}{dt} = & \frac{1}{2} \int_0^v N(v-v',t)N(v',t) \beta(v-v',v')dv' - \\ & \int_0^\infty N(v,t)N(v',t) \beta(v,v')dv' - \gamma(v)N(v,t) + \\ & \int_v^\infty \alpha(v,v')\gamma(v')N(v',t) dv' , \end{aligned} \quad (1)$$

1 where $N(v, t)$ is the number density distribution function representing the number of particles
2 per system volume with particle volume v at time t . $\beta(v, v')$ is the aggregation kernel. $\gamma(v)$
3 is the breakage rate kernel, $\alpha(v, v')$ is the breakage daughter size distribution function which
4 represents the probability of making a daughter volume v from a parent volume v' . The first
5 term on the right-hand side of the Eq. 1 calculates the birth rate of particle volume v due to
6 aggregation of particles smaller than particle volume v . The second term calculates the death
7 rate of particle volume v due to aggregation with other particles. The third term calculates the
8 death rate of particle volume v due to fragmentation. The final term calculates the birth rate of
9 particle volume v due to fragmentation of particles larger than particle volume v . A linear grid
10 ($v_i = iv_0$) can be used to discretize the Eq.1, which leads to the following formula [23-25],

$$\frac{dN_i}{dt} = \frac{1}{2} \sum_{j=1}^{i-1} N_j N_{i-j} \beta_{j,i-j} - N_i \sum_{j=1}^n N_j \beta_{i,j} - \gamma_i N_i + \sum_{j=i+1}^n \alpha_{ij} \gamma_j N_j \quad (2)$$

11 where the subscript i and j represent i th and j th discretized grid, respectively.

12 **2.2 Deep neural network**

13 Deep neural networks have been proven to be a powerful metamodeling tool and complex
14 function approximator [26]. Recent studies have shown that deep neural networks are a
15 promising and effective method to establish metamodel for approximating temporal response
16 of dynamical systems and approximating material constitute laws, which outperforms
17 traditional metamodeling techniques in terms of both the capability of capturing nonlinear
18 input-output relationships and prediction accuracy [27, 28]. In this work, a fully connected

1 deep feedforward neural network was used. In this network, the information passes forwardly
 2 from the input layer through several hidden layers to the output layer. Despite many other types
 3 of neural networks have been developed in the past decades, the feedforward neural network
 4 is simple yet effective. It has been shown to be sufficient for dealing with most of the partial
 5 differential equation problems [29, 30]. A L-layer neural network $f^L(\mathbf{x})$ can be written as
 6 follow,

$$\text{Input layer: } f^0(\mathbf{x}) = \mathbf{x} \in \mathbf{R}^{d_{in}}, \quad (3)$$

$$\text{Hidden layer: } f^l(\mathbf{x}) = \sigma(\mathbf{W}^l f^{l-1}(\mathbf{x}) + \mathbf{b}^l) \in \mathbf{R}^{f^l}, \quad (4)$$

$$\text{Output layer: } f^L(\mathbf{x}) = \mathbf{W}^L f^{L-1}(\mathbf{x}) + \mathbf{b}^L \in \mathbf{R}^{d_{out}}, \quad (5)$$

7 where \mathbf{x} is the input of the neural network, \mathbf{W}^l and \mathbf{b}^l are the weight matrix and bias vector in
 8 the l -th layer, respectively. σ is a non-linear activation function applied element-wisely. The
 9 feed forward neural network here consists of one input layer, $l-1$ hidden layers and one output
 10 layer.

11 **2.3 Physics-informed Neural network**

12 The schematic of the population balance embedded neural networks (PBNN) used in this work
 13 is shown in Figure 1. In this framework, a neural network $\hat{N}(\mathbf{x}; \boldsymbol{\theta})$ is firstly constructed to be
 14 a surrogate of the solution $N(\mathbf{x})$. Here $\boldsymbol{\theta}$ is the hyperparameters containing the set of all weight
 15 matrices \mathbf{W} and bias vectors \mathbf{b} in the neural network \hat{N} . An important feature of PBNN is that
 16 it respects the physical laws described by the population balance equations. This is achieved
 17 through modifying the loss function of the neural network. The governing equations are
 18 included as an additional term to punish the physical inconsistency of the output results of the
 19 neural network. One advantage of using a neural network as a surrogate model is that the
 20 derivative can be obtained through the chain rule for differentiating compositions of functions

1 in the optimization processes. The derivatives can be evaluated using backpropagation in a
2 deep neural network [31]. Herein, we use an automatic differentiation routine to compute the
3 derivatives of the network's outputs with respect to the network's inputs. It firstly applies a
4 forward pass to compute the values of all variables and then applies a backward pass to compute
5 the derivatives. Automatic differentiation provides an accurate and efficient way to calculate
6 derivatives, which has been implemented as a standard modular in most of the modern deep
7 learning frameworks [32]. On the one hand, the automatic differentiation algorithm provides a
8 robust way to update the hyperparameters in the neural network for optimization the trainings.
9 On the other hand, it also offers an opportunity to construct a physical constraint loss function
10 by directly incorporating the governing ordinary differential equations. Therefore, it has gained
11 significant attention in both the machine learning and physical modelling community.

12 In this work, the loss function of the neural network is constructed as follows,

$$L(\boldsymbol{\theta}) = \lambda_1 \left(\frac{1}{M_u} \sum_{i=1}^{M_u} |\hat{N}^i(\boldsymbol{\theta}) - N(x^i, t^i)|^2 \right) + \lambda_2 \left(\frac{1}{M_f} \sum_{i=1}^{M_f} |F(N^f)|^2 \right) \quad (6)$$

$$F(N_i) = \frac{dN_i}{dt} - \frac{1}{2} \sum_{j=1}^{i-1} N_j N_{i-j} \beta_{j,i-j} + N_i \sum_{j=1}^n N_j \beta_{i,j} + \gamma_i N_i - \sum_{j=i+1}^n \alpha_{ij} \gamma_j N_j \quad (7)$$

13 Here, M_u is the number of obersation points that are used to train the neural network; M_f is
14 the number of discretized grids that are used to approximate the particle size distribution. The
15 first term in the right-hand side of Eq. 6 represents the mean squared error of training data on
16 initial and observation training data. The second term is to punish the physics inconsistency
17 enforced by the population balance equation in Eq. 2. λ_1 and λ_2 are the regulation coefficients
18 to balance the weight of the two mean squared errors, respectively. They are chosen to be one
19 in this work. Note that the initial particle size distribution is imposed by hard constraint, i.e.

1 the output of the neural network is modified to the given initial particle size distribution during
2 each optimization step. It is found that hard constraints of initial and boundary conditions
3 significantly accelerate the optimization process and are very important for ensuring the
4 uniqueness of the learned solutions [33]. The optimization is first done through the widely used
5 stochastic gradient descent ADAM algorithm [34] to minimize the loss function. Later, a
6 second-order method L-BFGS is chosen in further optimization steps [35]. The L-BFGS
7 optimization is found to greatly improve training efficiency, particularly in solving inverse
8 problems.

9 **3. Simulation results**

10 In this section, two distinct problems will be studied. The first problem is to solve the
11 population balance equation in forward problem, which is to estimate the unknown hidden state
12 of the system given fixed model parameters. The second problem is data-driven discovery of
13 the population balance equation, which is to predict the model parameters that can best describe
14 the observation data. Analytical solutions of the studied cases are used to train the PBNN. The
15 effects of the neural network in PBNN will also be investigated. In general, a good combination
16 of the architecture of neural networks is important for achieving a robust prediction. After some
17 preliminary trials, a neural network architecture with 8 hidden layers (each layer has 20 neurons)
18 has been chosen for most of the studied cases. Hyperbolic tangent (tanh) is used as the
19 activation function of the neurons and Xavier normal initializer is used to set the initial random
20 weights of layers where initial weights are drawn from a truncated normal distribution [36].
21 The effects of the network on the performance will also be briefly discussed in the following
22 section.

1 3.1 Solving forward problem of the aggregation and breakage processes

2 Scott [37] presented an analytical solution for aggregation processes with a constant kernel and
3 various initial conditions. Here, the aggregation case with a Gaussian-like distribution as an
4 initial condition is solved. The initial condition is given as follows,

$$n(v, 0) = \frac{N_0}{v_0} \left(\frac{v}{v_0} \right) e^{-v/v_0} \quad (8)$$

5 The value N_0 and v_0 are the initial number of particles per unit volume and the initial mean
6 volume of the particles. The analytical solution for the number density function is given by Eq
7 9

$$n(v, t) = \frac{N_0}{v_0} \frac{4e^{-2\xi}}{\xi(T+2)^2} \sum_{k=1}^{\infty} \frac{(2\xi)^{2(k+1)}}{\Gamma(2(k+1))} \left(\frac{T}{T+2} \right)^k \quad (9)$$

8 where $\xi = v/v_0$. T is the non-dimensional time given by Eq 10

$$T = \beta_0 N_0 t \quad (10)$$

9 Here, β_0 is the aggregation rate constant. The analytical solution of the total number of particles
10 is provided as below.

$$N(t) = 2N_0/(T+2) \quad (11)$$

11 Since the analytical formulation is general, a benchmark case with $N_0 = 1$, $\beta_0 = 1$ and $v_0 =$
12 1 is investigated here. The volume of the smallest particle is considered to be 0.25 and a grid
13 with 40 particle size bins is used. The simulation time step is set to 0.01 and the aggregation
14 time between 0 and 1 second is modelled.

15 Figure 2 shows the loss of PBNN during the optimization process. It can be seen that the loss
16 continues to decrease as expected. A two-stage optimization process is adopted here. The first

1 2000 epoch optimization steps are achieved through the stochastic gradient descent ADAM
2 algorithm with learning rate of 0.1. It is found that there is a substantial decrease of the loss at
3 the beginning of the optimization while the decreasing rate becomes quite slow after 1000
4 epochs. To further speed up the optimization process, the optimization algorithm is switched
5 to a second-order L-BFGS method after 2000 epochs where there is a small jump of the loss
6 right after switching. Nevertheless, the loss drops sharply during the first 100 epochs of the L-
7 BFGS. After that, the decreasing rate of the loss becomes very slow due to the convergence of
8 the solutions, which is further confirmed through comparisons between the analytical solution
9 and the predicted number density function of the final time step as shown in Figure 3. It can be
10 seen that the predictions are getting closer to the analytical solution along with the optimization
11 process. The final prediction at 3000 epochs has excellent agreement with the analytical
12 solution.

13 The impacts of the depth of the neural network architecture on the loss and prediction are shown
14 in Figure 4. The neural networks have 20 neurons in each layer and three depths (i.e. 4 layers,
15 8 layers and 12 layers) are compared. In general, all three networks generate satisfactory
16 predictive performance, which indicates the robustness of the proposed approach. It is observed
17 that the 4 layers network results in a high oscillation during the first phase ADAM optimization
18 and produces a relatively less accurate prediction on the final particle size number density. In
19 comparison, a 12 layers network seems to produce the best prediction results. However, it
20 contains more parameters and thus needs more computational resources for training. As a rule
21 of thumb, it is usually preferable to choose the simplest network structure that can still achieve
22 a desired prediction performance. It is found that the 8 layers network produces almost the
23 same results as the 12 layers network. Table 1 lists a series of tests with different combinations
24 of numbers of hidden layers and neurons. The relative L2 error is calculated as $\epsilon =$

1 $\frac{\sqrt{\sum_{i=1}^M \|n_{pred}^i - n_{ana}^i\|^2}}{\sqrt{\sum_{i=1}^M \|n_{ana}^i\|^2}}$. In general, the error decreases when the network becomes wider (more
2 neurons per layer) and deeper (more hidden layers). However, the accuracy does not change
3 too much when the number of hidden layers is increasing from 8 to 12. Furthermore, there is
4 no significant improvement when using more than 20 hidden neurons per layer. Therefore, a
5 network of 8 hidden layers with 20 hidden neurons architecture is preferred in this work.

6 Figure 5 illustrates the final convergence of the number density function solution in terms of a
7 three-dimensional surface and a contour plot. Note that the solution from the traditional
8 Artificial Neural Network (ANN) method is also plotted. The ANN has the same neural
9 network setting as PBNN except that population balance equations are not encoded in the loss
10 function. The loss function of ANN only contains the root mean square error between the neural
11 network output and the analytical solution of the particle size distribution. The training is
12 performed by minimizing the loss function over multiple time steps. It can be seen that both
13 ANN and PBNN can successfully approximate a similar shape as the analytical solution. The
14 number of small particles decreases, and the number of larger particles increases with the
15 aggregation time. As shown in the contour plot, the aggregation process looks like the diffusion
16 of concentration field in a temporal evolution. However, it is obvious that there are some
17 discrepancies between the ANN and the analytical solution whereas the solution from PBNN
18 is closer to the analytical solution. To validate the prediction, Figure 6 compares the time
19 evolution of the total number of particles predicted by PBNN, ANN, method of class with 10
20 discretized bins and the analytical solution. It can be seen that the PBNN predicts that the
21 number of particles decreases with the aggregation time, which is in a very good agreement
22 with the analytical solution. In comparison, the solution with the method of class slightly
23 overestimates the total number of particles through the aggregation process. In addition, the
24 prediction of ANN deviates significantly from the analytical solution, which indicates that the

1 conservation law is difficult to maintain using ANN although it can approximate the shape of
 2 the solution. By training with more numerical results obtained from different sets of parameters
 3 may help improve the predictions of ANN. However, this requires more computational
 4 resources and it still could not guarantee that the physical constraints of the distribution are
 5 met. Figure 7 further shows that the predictions of the particle size distribution at different
 6 aggregation time agree with the analytical solution, highlighting that the dynamic evolution of
 7 the aggregation process is correctly captured.

8 Ziff and McGrady [38] derived an analytical solution for a uniform binary breakup case. The
 9 breakage kernel and the daughter particle distribution function are given as below.

$$\gamma = v^2 \quad (12)$$

$$\alpha(v, v') = 2/v' \quad (13)$$

10 In this particular case, the initial particle number distribution function is set to be
 11 monodispersed, i.e. $n(v, 0) = \delta(v - v_0)$. The analytical solution of particle number density
 12 distribution is given by

$$n(v, t) = e^{-tv^2} [\delta(v - v_0) + 2tv_0\Theta(v_0 - v)] \quad (14)$$

13 where Θ is the step function. The total number of particles can be obtained by integrating the
 14 number density distribution. The initial particle size v_0 is set to 1 in this case. The volume of
 15 the smallest particle is considered to be 0.25 and a grid of 40 particle size bins is used.

16 Figure 8 presents a comparison of the numerical and analytical solutions for the variation of
 17 the total number of particles. It is confirmed that the total number of particles is increasing
 18 during a breakage process and the predictions of PBNN almost overlap with the analytical
 19 solutions. The predictions from the method of class with 10 discretized bins slightly

1 overestimate the total number of particles throughout the breakage process and there is a
2 distinct deviation between the predictions from ANN and analytical solution. Furthermore,
3 Figure 9 shows that the predictions of the trajectories of particle number density function by
4 PBNN are in a good agreement with the analytical results. These results indicate that the time
5 evolution of particle number density function during the breakage process is well predicted by
6 the present PBNN method.

7 **3.2 Data-driven discovery of model parameters**

8 As mentioned in the introduction, inverse problems of particle aggregation and breakage
9 process are challenging to handle using existing methods. Therefore, it is worth exploring the
10 applicability of using PBNN to solve inverse problems. The problem studied here can also be
11 stated as the identifications of the parameters that best describe the provided observation data.
12 To estimate the parameters, the unknown parameters in the equation are treated as network
13 parameters that change during the optimization phase. This is achieved by defining them as
14 trainable variable objects in TensorFlow [39].

15 To demonstrate the applicability of the constructed framework, the analytical solutions of the
16 cases in section 3.1 are used as training data. Meanwhile, the aggregation and breakage rate
17 constants are not given in advance but are defined as variables for the program to estimate.
18 Figure 10 shows the evolution of the convergence in the model parameter identification process.
19 Notably, the estimated parameters converge to the true values of kernel parameters in both
20 aggregation and breakage cases. Meanwhile, it can be seen that the optimization is quite
21 efficient, i.e. the true kernel parameters are estimated with around 1000 epochs.

22 In a realistic process, there are inherently noises in the experimental observation data due to
23 the uncertainties in the measurement equipment, intrinsic variety of the particulate properties,
24 and complexity of the processes. To further consider this effect and test the power of the

1 proposed PBNN framework, we deliberately add some Gaussian white noise $G(0, \sigma)$ to the
2 training data of the aggregation case for increasing the estimation difficulty of the kernel
3 parameters. Here, G is a normal distribution with a standard deviation σ . Table 2 presents the
4 comparisons between the true value and the final estimated values with different levels of
5 Gaussian noises. It is found that the accuracy of the prediction decreases with the increase of
6 the magnitude of the noises. Nevertheless, the aggregation rate constant can still be estimated
7 reasonably well even with large noisy data. Theoretically, the framework can also be used to
8 denoise the experimental measurements and estimate the uncertainties. However, this is beyond
9 the scope of the present study but will be investigated in our future work.

10 To further demonstrate the model's applicability, the proposed PBNN approach is used to
11 determine the milling parameters of a platinum group minerals ore material in a laboratory test.
12 The material was milled in a Wits pilot under a rotating speed of 60 rpm [40]. The mono size
13 feed samples were prepared by sieving 2 kg from the 15 kg platinum ore batches. The size of
14 the feed material is in the range of 600-850 micron. To investigate the milling particle size
15 evolution, some kernel function closures in PBNN need to be defined. An empirical selection
16 function proposed by Austin, Klimpel and Luckie [41] is used to calculate the breakage rate.
17 The formula is given as follows,

$$\gamma = a \cdot v^\varepsilon \cdot \frac{1}{1 + \left(\frac{v}{\mu}\right)^\Lambda} \quad (15)$$

18 where a and μ are two parameters that depend on the mill operational conditions, ε and Λ are
19 two parameters that depend on the properties of milling materials. The breakage daughter size
20 distribution is calculated as follows [41],

$$B(v, v') = \phi \left(\frac{v}{v'}\right)^\varphi + (1 - \phi) \left(\frac{v}{v'}\right)^\omega \quad (16)$$

$$\alpha(v, v') = \frac{\partial B(v, v')}{\partial v} \quad (17)$$

1 where $B(v, v')$ is the cumulative breakage distribution function, φ and ω are two power index
 2 related to material characteristics, ϕ is also a material-dependent parameter representing the
 3 fraction of fines that will be produced in a single fracture step. In total, there are seven
 4 parameters to be estimated, which includes four breakage rate parameters (a, μ, ε and Λ) and
 5 three breakage daughter size distribution parameters (ϕ, φ and ω). All the seven parameters
 6 are set to be trainable variables in PBNN. The value ϕ is limited to vary from 0 to 1 while the
 7 other parameters are constrained to able to change from 0 to 10. The milling particle size
 8 distributions from 0 to 30 minutes are used to estimate the parameters.

9 Th final estimated parameters from PBNN are listed in Table 3. Figure 11 shows the
 10 comparison between measured and predicted particle size distribution evolution. It is found
 11 that there are some quantitative discrepancies of the particle size distribution in the early
 12 milling time, which may be due to the uncertainties in the function form of breakage kernel or
 13 the variability in the experiments. In general, a good match between the predicted and the
 14 experimentally measured particle size distribution evolution is observed. Generally, the
 15 physics-informed neural-network approach is deemed as a data-efficient machine learning
 16 method since the underlying laws of physics are explicitly encoded [19, 42, 43]. In practice,
 17 with the increase of the complexity of the kernel functions, PBNN may need more data to
 18 improve the model capability.

19 **4. Conclusion**

20 In this work, a physics-informed deep learning approach is developed for solving and
 21 discovering particle aggregation and breakage processes. The governing equations of the

1 population balance model are incorporated into the loss function of a neural network by taking
2 advantage of the recently proposed advanced automatic differentiation algorithm. The
3 embedding of physical constraints makes it more efficient to train the neural network and
4 achieve reliable predictions. Compared with classical methods for modeling particle
5 aggregation and breakage processes, the proposed population balance neural network approach
6 can be used to solve both forward and inverse problems. The impact of the depth of the network
7 on the final predictions is also analysed. A shallow network is found to produce an oscillation
8 of loss during the optimization process and a deeper network can help increase the accuracy of
9 the predictions. It is demonstrated that the proposed approach can match well the analytical
10 solutions available in the literature. It is also shown that the kernel parameters in the reverse
11 problem can be successfully identified even with noisy observation data. Furthermore, the
12 method is used to determine the preliminary parameters from a pilot-scale milling experiment.
13 A good match between the predicted and the experimentally measured particle size distribution
14 evolution is observed.

15 Although training data is not a prerequisite in the forward problem of a physics-informed neural
16 network based approach, most of the current applications still use labeled data to help the
17 network converge [19, 29, 42, 43]. In practice, we also found that the network converges faster
18 with the aid of analytical solutions as labeled data in the forward problem. Noteworthy, some
19 very recent works have been able to use physics-informed neural network based approach
20 without labeled data [33, 44, 45]. Therefore, such methods will be explored for dealing with
21 more complexed kernels in our future work. Another limitation of the current PBNN is that it
22 can only be used to predict the undetermined parameters of several candidate kernel equations.
23 As for future work, it would be beneficial to use the method to discover closure formulation
24 for kernel functions, which could be achieved with the aid of recently proposed advanced
25 symbolic regression [46] or sparse identification of nonlinear dynamics framework [47].

1 Furthermore, the physics-informed neural network approach has shown to be successful in
2 solving fluid flow problems like a meshless CFD solver [19, 33, 43, 44]. Therefore, we will
3 investigate the possibility to extend the current work to implement a physics-informed neural
4 network based CFD-PBM solver to deal with more complicate particulate processes.

5 **Acknowledgments**

6 The first author would like to acknowledge the startup funding from University College Cork.
7 The corresponding author would like to thank Innovate UK for funding the Knowledge
8 Transfer Partnership between University of Sheffield and Process Systems Enterprise. The
9 MIT xPRO course Machine Learning, Modelling and Simulation Principles delivered by Prof.
10 Youssef Marzouk from MIT is highly appreciated and inspirational to conceptualize this work.

11 **Nomenclature**

a	Fitting parameter, -
b	Bias vector of neural network, -
B	Cumulative breakage distribution function, -
f	Neural network, -
F	Physics inconsistency of the surrogate solution, -
L	Loss function, -
M_u	Number of observation points, -
M_f	Number of discretized grids, -

N	Number density distribution function, m^{-6}
\hat{N}	Surrogate solution, m^{-6}
t	Time, s
T	Non-dimensional time, -
v	Particle volume, m^3
W	weight matrix of neural network, -
x	Input of neural network, m^{-6}

1

2 **Greek letters**

α	Breakage daughter size distribution
β	Aggregation kernel
γ	Breakage rate kernel
λ	Regulation coefficient
μ	Fitting parameter
ε	Material fitting parameter
ϵ	Relative error
φ	Material fitting parameter

ω	Material fitting parameter
θ	Hyperparameters
ξ	Non-dimensional particle volume
δ	Delta function
Λ	Material fitting parameter
\emptyset	Material fitting parameter
Γ	Gamma function
Θ	Step function

1

2 Reference

- 3 [1] D. Ramkrishna, Population balances: Theory and applications to particulate systems in
4 engineering, Elsevier2000.
- 5 [2] C.D. Immanuel, F.J. Doyle III, Solution technique for a multi-dimensional population
6 balance model describing granulation processes, Powder Technology 156 (2005) 213-225.
- 7 [3] X. Chen, L.G. Wang, J.Y. Ooi, A DEM-PBM multiscale coupling approach for the
8 prediction of an impact pin mill, Powder Technology (2020).
- 9 [4] B. Olaleye, C.-Y. Wu, L.X. Liu, Impact of feed material properties on the milling of
10 pharmaceutical ribbons: A PBM analysis, International Journal of Pharmaceutics (2020)
11 119954.
- 12 [5] C.Y. Ma, X.Z. Wang, K.J. Roberts, Morphological population balance for modeling crystal
13 growth in face directions, AIChE journal 54 (2008) 209-222.
- 14 [6] Z. Li, L.G. Wang, W. Chen, X. Chen, C. Liu, D. Yang, Scale-up procedure of parameter
15 estimation in selection and breakage functions for impact pin milling, Advanced Powder
16 Technology 31 (2020) 3507-3520.
- 17 [7] X.Z. Chen, Z.H. Luo, W.C. Yan, Y.H. Lu, I.S. Ng, Three-dimensional CFD-PBM coupled
18 model of the temperature fields in fluidized-bed polymerization reactors, AIChE Journal 57
19 (2011) 3351-3366.
- 20 [8] T. Wang, J. Wang, Y. Jin, Population balance model for gas– liquid flows: Influence of
21 bubble coalescence and breakup models, Industrial & engineering chemistry research 44 (2005)
22 7540-7549.

- 1 [9] Z. Gao, D. Li, A. Buffo, W. Podgórska, D.L. Marchisio, Simulation of droplet breakage in
2 turbulent liquid–liquid dispersions with CFD-PBM: comparison of breakage kernels, *Chemical*
3 *Engineering Science* 142 (2016) 277-288.
- 4 [10] X. Yu, M.J. Hounslow, G.K. Reynolds, A. Rasmuson, I. Niklasson Björn, P.J.
5 Abrahamsson, A compartmental CFD-PBM model of high shear wet granulation, *AICHE*
6 *Journal* 63 (2017) 438-458.
- 7 [11] M. Hounslow, R. Ryall, V. Marshall, A discretized population balance for nucleation,
8 growth, and aggregation, *AICHE journal* 34 (1988) 1821-1832.
- 9 [12] D.L. Marchisio, J.T. Piktorna, R.O. Fox, R.D. Vigil, A.A. Barresi, Quadrature method of
10 moments for population-balance equations, *AICHE Journal* 49 (2003) 1266-1276.
- 11 [13] J. Su, Z. Gu, Y. Li, S. Feng, X.Y. Xu, Solution of population balance equation using
12 quadrature method of moments with an adjustable factor, *Chemical Engineering Science* 62
13 (2007) 5897-5911.
- 14 [14] Y. Lin, K. Lee, T. Matsoukas, Solution of the population balance equation using constant-
15 number Monte Carlo, *Chemical Engineering Science* 57 (2002) 2241-2252.
- 16 [15] S. Alzyod, S. Charton, A meshless Radial Basis Method (RBM) for solving the detailed
17 population balance equation, *Chemical Engineering Science* (2020) 115973.
- 18 [16] M. Shiea, A. Buffo, M. Vanni, D. Marchisio, Numerical Methods for the Solution of
19 Population Balance Equations Coupled with Computational Fluid Dynamics, *Annual Review*
20 *of Chemical and Biomolecular Engineering* 11 (2020) 339-366.
- 21 [17] N. Baker, F. Alexander, T. Bremer, A. Hagberg, Y. Kevrekidis, H. Najm, M. Parashar, A.
22 Patra, J. Sethian, S. Wild, Workshop report on basic research needs for scientific machine
23 learning: Core technologies for artificial intelligence, USDOE Office of Science (SC),
24 Washington, DC (United States), 2019.
- 25 [18] S. Rudy, A. Alla, S.L. Brunton, J.N. Kutz, Data-driven identification of parametric partial
26 differential equations, *SIAM Journal on Applied Dynamical Systems* 18 (2019) 643-660.
- 27 [19] M. Raissi, P. Perdikaris, G.E. Karniadakis, Physics-informed neural networks: A deep
28 learning framework for solving forward and inverse problems involving nonlinear partial
29 differential equations, *Journal of Computational Physics* 378 (2019) 686-707.
- 30 [20] J. Han, A. Jentzen, E. Weinan, Solving high-dimensional partial differential equations
31 using deep learning, *Proceedings of the National Academy of Sciences* 115 (2018) 8505-8510.
- 32 [21] D. Zhang, L. Lu, L. Guo, G.E. Karniadakis, Quantifying total uncertainty in physics-
33 informed neural networks for solving forward and inverse stochastic problems, *Journal of*
34 *Computational Physics* 397 (2019) 108850.
- 35 [22] Y. Bar-Sinai, S. Hoyer, J. Hickey, M.P. Brenner, Learning data-driven discretizations for
36 partial differential equations, *Proceedings of the National Academy of Sciences* 116 (2019)
37 15344-15349.
- 38 [23] R. Charls, Energy-size reduction relationships in comminution, *Trans. AIME* 9 (1957) 80-
39 88.
- 40 [24] D. Fuerstenau, A.-Z. Abouzeid, The energy efficiency of ball milling in comminution,
41 *International Journal of Mineral Processing* 67 (2002) 161-185.
- 42 [25] G.M. Hidy, On the theory of the coagulation of noninteracting particles in Brownian
43 motion, *Journal of Colloid Science* 20 (1965) 123-144.
- 44 [26] S. Chen, S. Billings, Neural networks for nonlinear dynamic system modelling and
45 identification, *International journal of control* 56 (1992) 319-346.
- 46 [27] D.J. Fonseca, D.O. Navarrese, G.P. Moynihan, Simulation metamodeling through
47 artificial neural networks, *Engineering applications of artificial intelligence* 16 (2003) 177-183.
- 48 [28] K. Wang, W. Sun, Meta-modeling game for deriving theory-consistent, microstructure-
49 based traction–separation laws via deep reinforcement learning, *Computer Methods in Applied*
50 *Mechanics and Engineering* 346 (2019) 216-241.

- 1 [29] L. Lu, X. Meng, Z. Mao, G.E. Karniadakis, DeepXDE: A deep learning library for solving
2 differential equations, arXiv preprint arXiv:1907.04502 (2019).
- 3 [30] Z. Liu, Y. Yang, Q.-D. Cai, Solving Differential Equation with Constrained Multilayer
4 Feedforward Network, arXiv preprint arXiv:1904.06619 (2019).
- 5 [31] D.E. Rumelhart, G.E. Hinton, R.J. Williams, Learning representations by back-
6 propagating errors, *nature* 323 (1986) 533-536.
- 7 [32] A.G. Baydin, B.A. Pearlmutter, A.A. Radul, J.M. Siskind, Automatic differentiation in
8 machine learning: a survey, *The Journal of Machine Learning Research* 18 (2017) 5595-5637.
- 9 [33] L. Sun, H. Gao, S. Pan, J.-X. Wang, Surrogate modeling for fluid flows based on physics-
10 constrained deep learning without simulation data, *Computer Methods in Applied Mechanics*
11 *and Engineering* 361 (2020) 112732.
- 12 [34] D.P. Kingma, J. Ba, Adam: A method for stochastic optimization, arXiv preprint
13 arXiv:1412.6980 (2014).
- 14 [35] D.C. Liu, J. Nocedal, On the limited memory BFGS method for large scale optimization,
15 *Mathematical programming* 45 (1989) 503-528.
- 16 [36] K. He, X. Zhang, S. Ren, J. Sun, Delving deep into rectifiers: Surpassing human-level
17 performance on imagenet classification, *Proceedings of the IEEE international conference on*
18 *computer vision*, 2015, pp. 1026-1034.
- 19 [37] W.T. Scott, Analytic studies of cloud droplet coalescence I, *Journal of the atmospheric*
20 *sciences* 25 (1968) 54-65.
- 21 [38] R.M. Ziff, E. McGrady, The kinetics of cluster fragmentation and depolymerisation,
22 *Journal of Physics A: Mathematical and General* 18 (1985) 3027.
- 23 [39] M. Abadi, A. Agarwal, P. Barham, E. Brevdo, Z. Chen, C. Citro, G.S. Corrado, A. Davis,
24 J. Dean, M. Devin, TensorFlow: Large-scale machine learning on heterogeneous systems,
25 (2015).
- 26 [40] N. Chimwani, D. Glasser, D. Hildebrandt, M.J. Metzger, F.K. Mulenga, Determination of
27 the milling parameters of a platinum group minerals ore to optimize product size distribution
28 for flotation purposes, *Minerals Engineering* 43 (2013) 67-78.
- 29 [41] L.G. Austin, R.R. Klimpel, P.T. Luckie, Process engineering of size reduction: ball milling,
30 Society of Mining Engineers of the American Institute of Mining, Metallurgical and Petroleum
31 Engineers 1984.
- 32 [42] M. Raissi, G.E. Karniadakis, Hidden physics models: Machine learning of nonlinear
33 partial differential equations, *Journal of Computational Physics* 357 (2018) 125-141.
- 34 [43] M. Raissi, A. Yazdani, G.E. Karniadakis, Hidden fluid mechanics: Learning velocity and
35 pressure fields from flow visualizations, *Science* 367 (2020) 1026-1030.
- 36 [44] C. Rao, H. Sun, Y. Liu, Physics-informed deep learning for incompressible laminar flows,
37 *Theoretical and Applied Mechanics Letters* 10 (2020) 207-212.
- 38 [45] O. Hennigh, S. Narasimhan, M.A. Nabian, A. Subramaniam, K. Tangsali, M. Rietmann,
39 J.d.A. Ferrandis, W. Byeon, Z. Fang, S. Choudhry, NVIDIA SimNetTM: an AI-accelerated
40 multi-physics simulation framework, arXiv preprint arXiv:2012.07938 (2020).
- 41 [46] S.-M. Udrescu, M. Tegmark, AI Feynman: A physics-inspired method for symbolic
42 regression, *Science Advances* 6 (2020) eaay2631.
- 43 [47] S.L. Brunton, J.L. Proctor, J.N. Kutz, Discovering governing equations from data by
44 sparse identification of nonlinear dynamical systems, *Proceedings of the national academy of*
45 *sciences* 113 (2016) 3932-3937.

46

47

1 **Figure Captions**

2 Figure 1. Diagram of a population balance neural network (PBNN) model for solving the
3 forward and inverse problems of particle aggregation and breakage systems.

4 Figure 2 The optimization process of PBNN for solving the aggregation case

5 Figure 3 The prediction of the particle number density during the optimization process. (a) 200
6 epochs (b) 1000 epochs (c) 2000 epochs (d) 3000 epochs

7 Figure 4 Effect of the depth of the neural network architecture on the loss and prediction results
8 in the aggregation case. (a) Loss function during optimization (b) Comparisons between the
9 predictions and the analytical solution of final size number density.

10 Figure 5. Solution of the number density function in the aggregation case

11 Figure 6 Comparison between the prediction of total number of particles evolution and the
12 analytical solution in aggregation case.

13 Figure 7. Comparison of the predictions and the analytical solutions of the time evolution of
14 particle number density in aggregation case

15 Figure 8 Comparison between the prediction of total number of particles evolution and the
16 analytical solution in the breakage case.

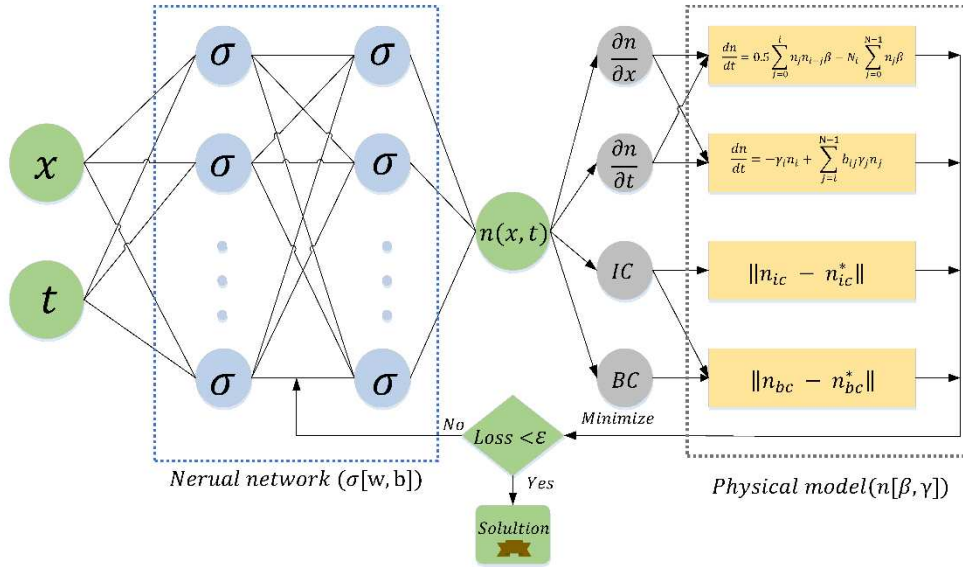
17 Figure 9 Comparison of the predictions and the analytical solutions of the time evolution of
18 particle number density in the breakage case

19 Figure 10 Kernel parameter estimations by PBNN (a) aggregation rate constant estimation (b)
20 breakage rate constant estimation

21 Figure 11 Measured and predicted particle size distributions in a ball milling laboratory test

22

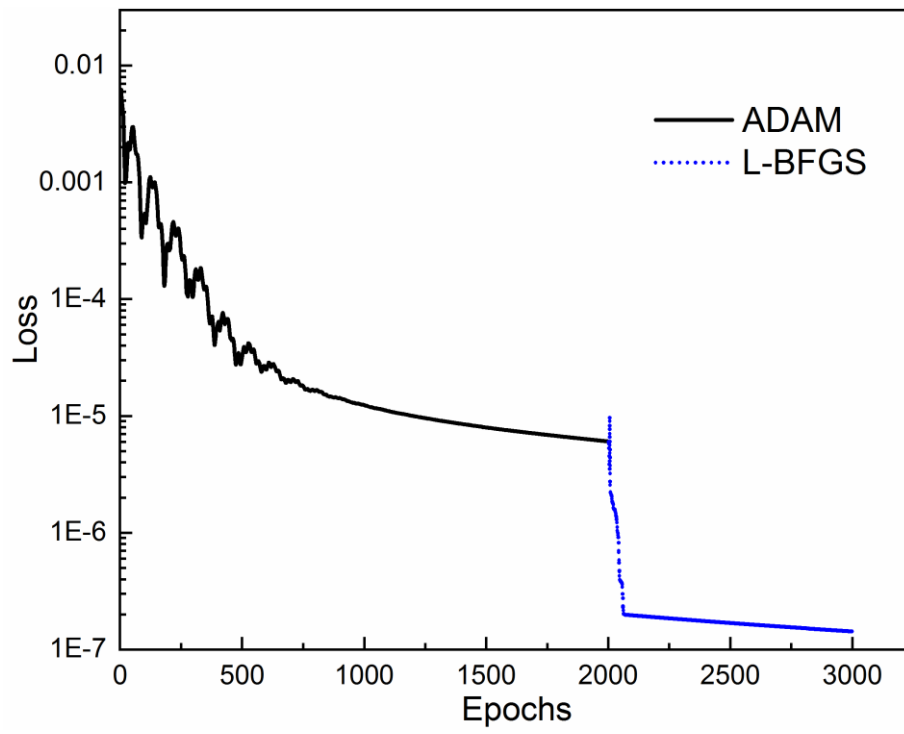
23



1

2 Figure 1. Diagram of a population balance neural network (PBNN) model for solving the
 3 forward and inverse problems of particle aggregation and breakage systems.

4

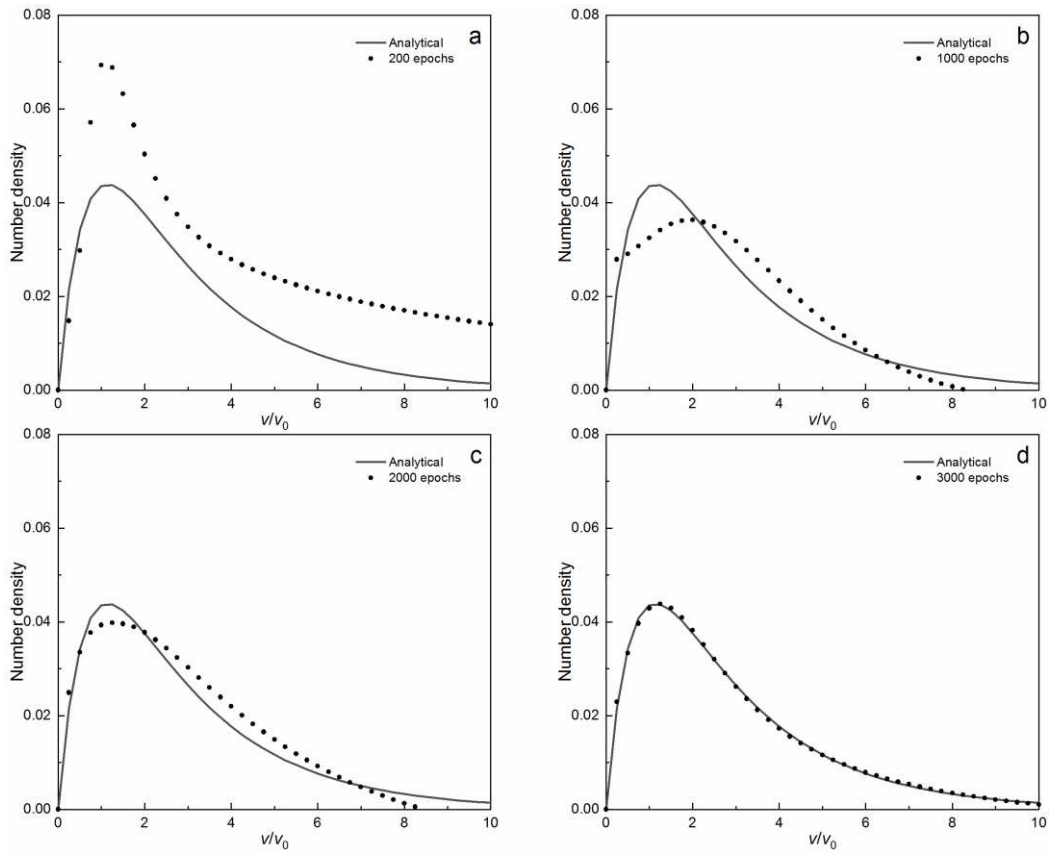


1

2

Figure 2 The optimization process of PBNN for solving the aggregation case

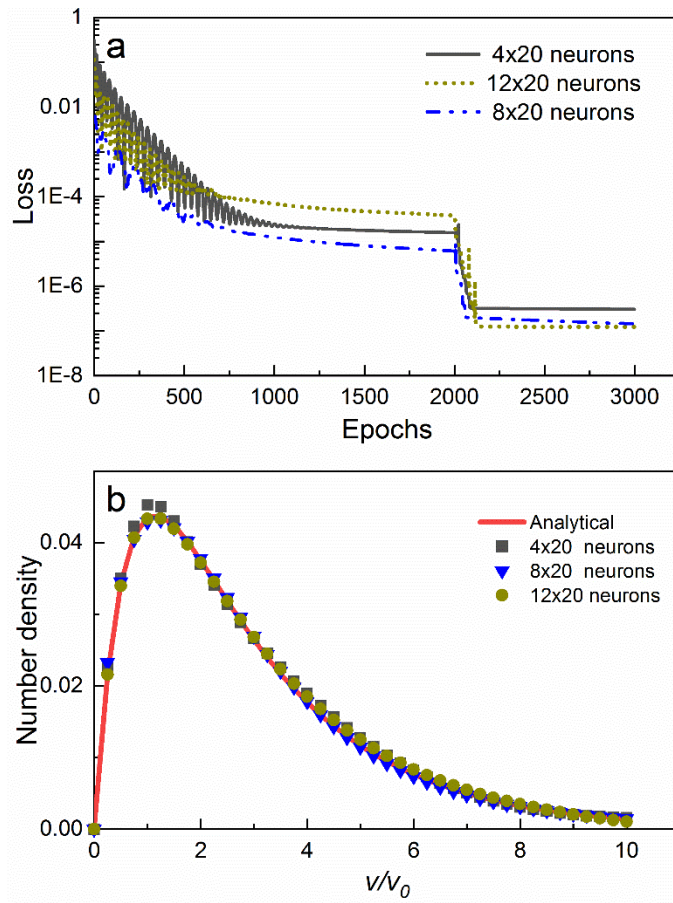
3



1

2 Figure 3 The prediction of the particle number density during the optimization process. (a)
 3 200 epochs (b) 1000 epochs (c) 2000 epochs (d) 3000 epochs

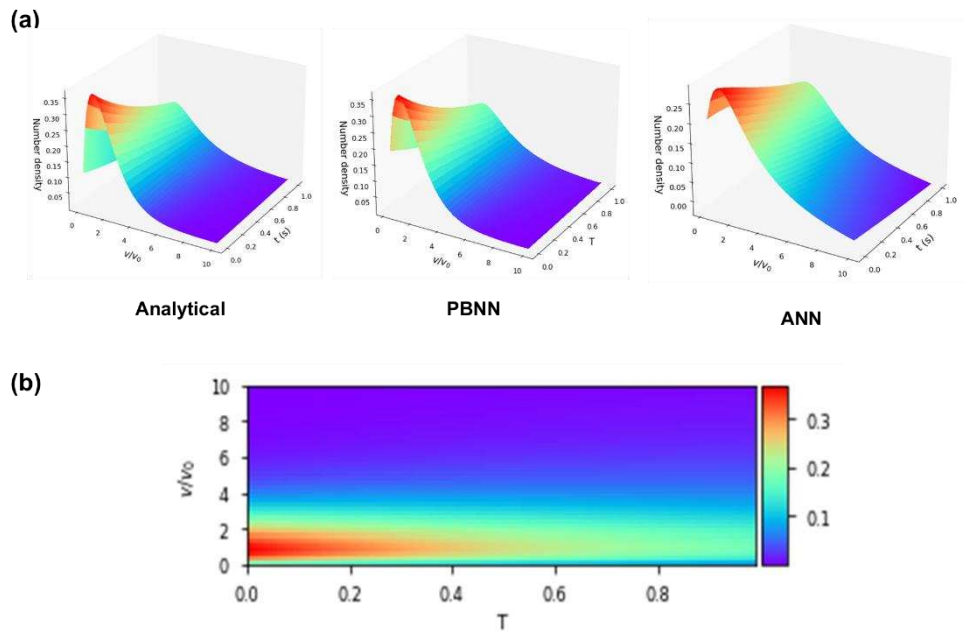
4



1
2
3
4
5

Figure 4 Effect of the depth of the neural network architecture on the loss and prediction results in the aggregation case. (a) Loss function during optimization (b) Comparisons between the predictions and the analytical solution of final size number density.

1



2

3

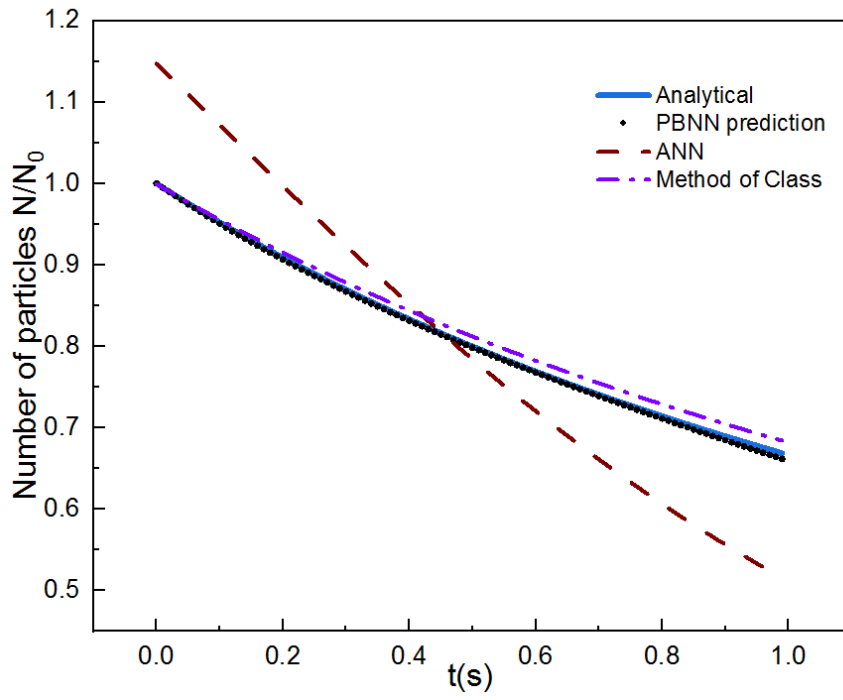
Figure 5. Solution of the number density function in the aggregation case

4

(a) surface plot from Analytical solution, PBNN and ANN (b) contour plot from PBNN

5

1



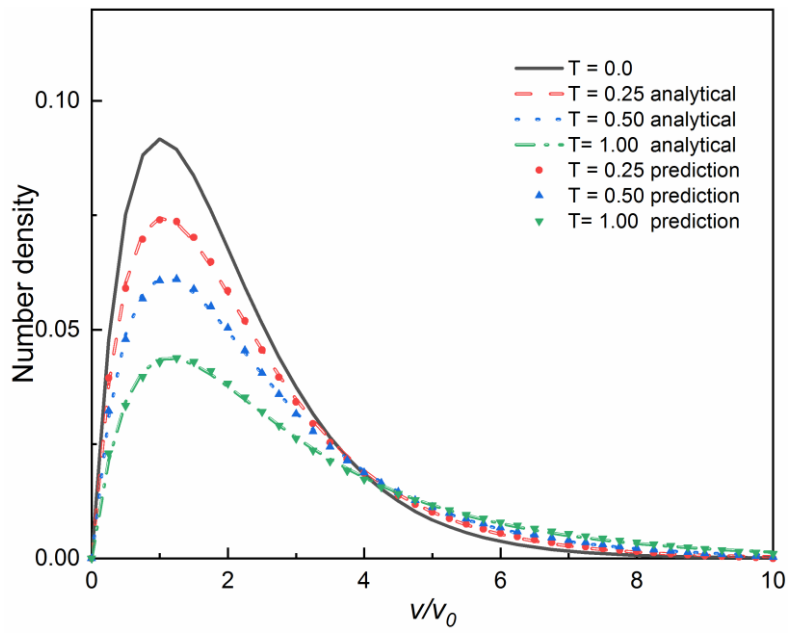
2

3

Figure 6 Comparison between the prediction of total number of particles evolution and the analytical solution in aggregation case.

4

5

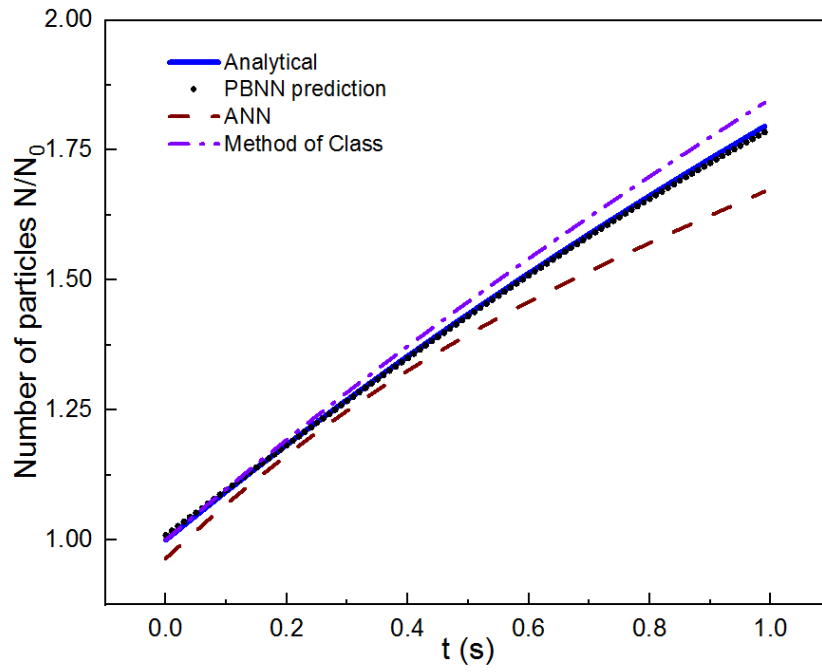


1

2 Figure 7. Comparison of the predictions and the analytical solutions of the time evolution of
 3 particle number density in aggregation case

4

1



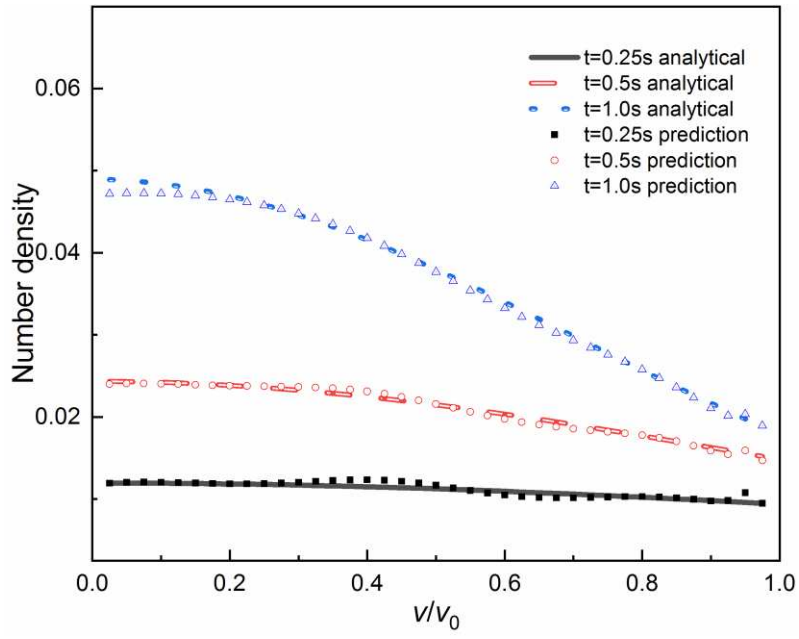
2

3

Figure 8 Comparison between the prediction of total number of particles evolution and the analytical solution in the breakage case.

4

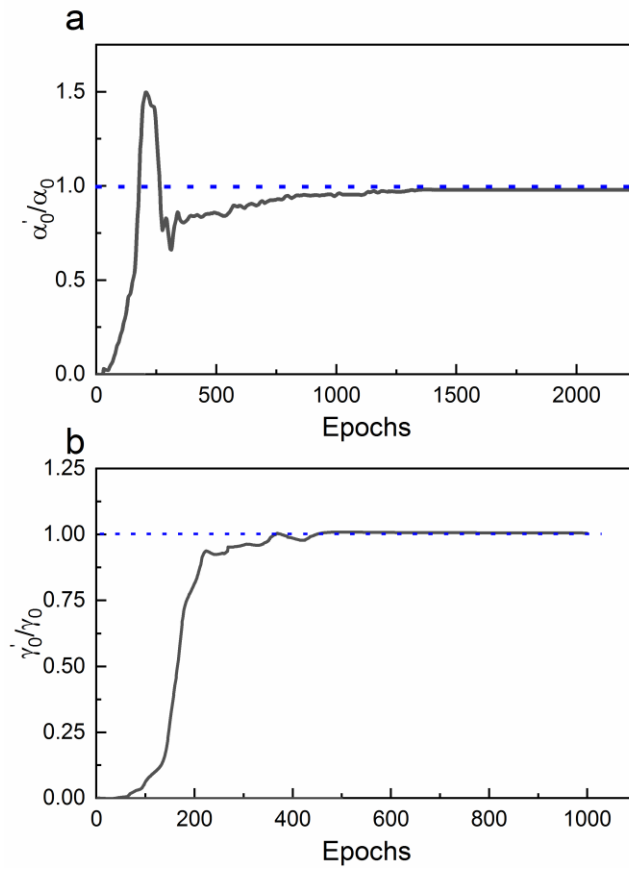
5



1

2 Figure 9 Comparison of the predictions and the analytical solutions of the time evolution of
 3 particle number density in the breakage case

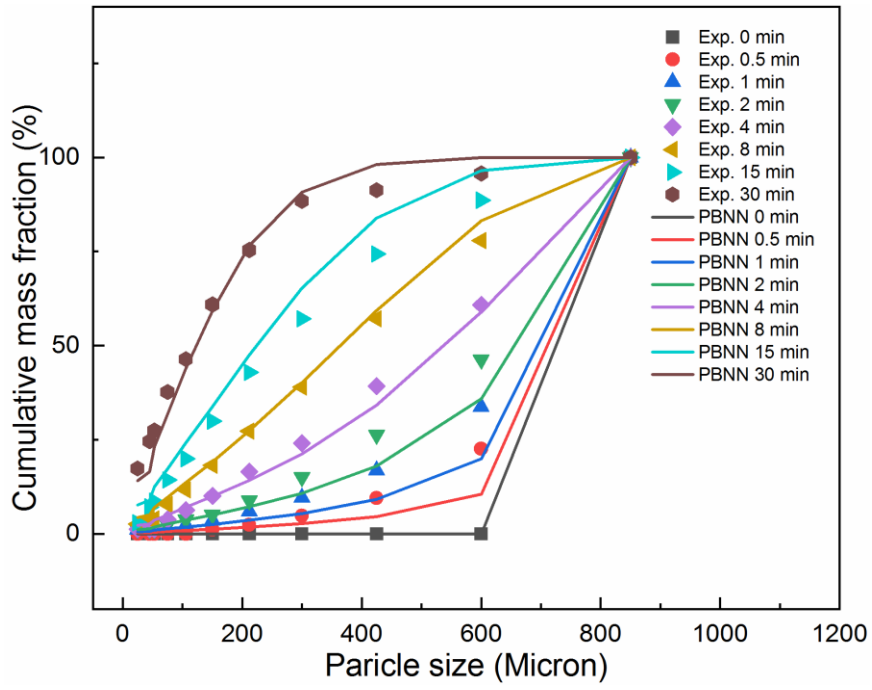
4



1

2 Figure 10 Kernel parameter estimations by PBNN (a) aggregation rate constant estimation (b)
 3 breakage rate constant estimation

4



1

2 Figure 11 Measured and predicted particle size distributions in a ball milling laboratory test

3

1 **Table captions**

2 Table 1 Relative L2 errors of the predictions with varying layer widths and depths of the neural
3 network

4 Table 2 Kernel parameter estimation with noise training data (true value =1)

5 Table 3 Kernel parameter estimation in the ball milling laboratory test

6

7

1 **Table 1** Relative L2 errors of the predictions with varying layer widths and depths of the neural
2 network

Width \ Depth	4	8	12
10	4.92×10^{-2}	2.34×10^{-2}	2.45×10^{-2}
20	1.96×10^{-2}	1.26×10^{-2}	1.24×10^{-2}
40	1.67×10^{-2}	1.21×10^{-2}	1.22×10^{-2}

3

1

Table 2 Kernel parameter estimation with noise training data (true value =1)

Noise	$\sigma = 0$	$\sigma = 0.01$	$\sigma = 0.05$	$\sigma = 0.07$	$\sigma = 0.1$
PBNN Estimation	1.000	0.998	0.992	0.972	0.94

2

3

1

2

Table 3 Kernel parameter estimation in the ball milling laboratory test

variable	a	ε	Λ	μ	\emptyset	φ	ω
PBNN Estimation	0.27	1.14	7.95	7.26	0.57	4.88	0.95

3